Offshore Rayleigh group velocity observations of the South Island, New Zealand, from ambient noise data

William L. Yeck,[1,*] Anne F. Sheehan,[1] Joshua C. Stachnik[2] and Fan-Chi Lin[3]

[1] *CIRES and Department of Geological Sciences, University of Colorado at Boulder, CO 80309, USA. E-mail: William.Yeck@colorado.edu*
[2] *Department of Earth and Environmental Sciences, Lehigh University, Bethlehem, PA 18015, USA*
[3] *Department of Geology and Geophysics, University of Utah, Salt Lake City, UT 84112, USA*

SUMMARY

We present azimuthally anisotropic Rayleigh group velocity models from 8 to 35 s both offshore and onshore of the South Island of New Zealand. We use MOANA (Marine Observations of Anisotropy Near Aotearoa) broad-band ocean seismic data in combination with on land data from the New Zealand National Seismography Network to investigate the seismic structure of the flanks of the Australian–Pacific plate boundary. At 8 s, we observe low offshore group velocities best explained by the influence of the water layer and thick water-laden sediments. At long periods (20–30 s), group velocities are lower on the South Island relative to its offshore flanks, due to thickened crust beneath the island, with the lowest velocities primarily beneath the Southern Alps. Group velocity azimuthal anisotropy fast directions near the Alpine Fault align with the direction of relative plate motion between the Australian and Pacific plates. In the southern portion of the island, fast directions rotate anticlockwise, likely in response to a decrease in dextral shearing away from the plate boundary. Azimuthal anisotropy fast directions align with absolute plate motion offshore on the Pacific plate. Based on the depth sensitivity of our observations, we suggest diffuse deformation occurs throughout the crust. Our observations match trends in previous Pn anisotropy and SKS shear wave splitting observations, and therefore suggest a consistent pattern of distributed deformation throughout the lithosphere.

Key words: Tomography; Surface waves and free oscillations; Seismic anisotropy; Continental tectonics: strike-slip and transform; Crustal structure; New Zealand.

1 INTRODUCTION

The South Island of New Zealand marks the transform boundary between the Pacific and Australian plate. The major surface expression of the plate boundary is the Alpine Fault, a northeast striking fault that splits the South Island longitudinally (Fig. 1). The Alpine Fault is a dextral, oblique strike-slip fault. At present, the Alpine Fault accommodates ∼70 per cent of plate motion and has been estimated to have accommodated greater than ∼50 per cent of displacement in the past 45 Ma (Sutherland *et al.* 2000). While strike-slip deformation is observable on the surface, there remain questions as to how strain is accommodated at depth. Recent studies targeted this question relying on seismic (Collins & Molnar 2014; Zietlow *et al.* 2014; Karalliyadda *et al.* 2015), or a combinations geodetic and seismic observations (Houlié & Stern 2012). These studies use measurements of seismic anisotropy that are sensitive to the lower crust and

mantle, relying on observations of anisotropy from primarily relatively deep (>35 km) local earthquakes (Karalliyadda & Savage 2013), Pn anisotropy (Collins & Molnar 2014), or SKS shear wave splitting measurements (Zietlow *et al.* 2014). In this paper, we investigate azimuthal anisotropy in the crust through Rayleigh group velocity dispersion measurements derived from ambient noise.

The modern surface expression of the plate boundary is well documented on-land from GPS data. Maximum strain rates occur west of Canterbury, along the eastern edge of the Alpine Fault (Beavan & Haines 2001). Strike-slip rates along the Alpine Fault, derived from block-model inversions of geodetic data, reach 31 mm yr^{-1} on the central portion of the South Island, and are generally smaller north of the Hope-Alpine Fault junction (∼5 mm yr^{-1}) (Wallace *et al.* 2007). This maximum geodetically derived strike-slip rate slightly exceeds that constrained by geological data (27 ± 5 mm yr^{-1}) (Norris & Cooper 2001). The central portion of the Alpine Fault has a significant convergent component (Wallace *et al.* 2007), which agrees with observed positive vertical GPS motion west of the fault (Houlié & Stern 2012). The continental crust is thickened below the South Island with the crust–mantle boundary, or Moho, at depths of

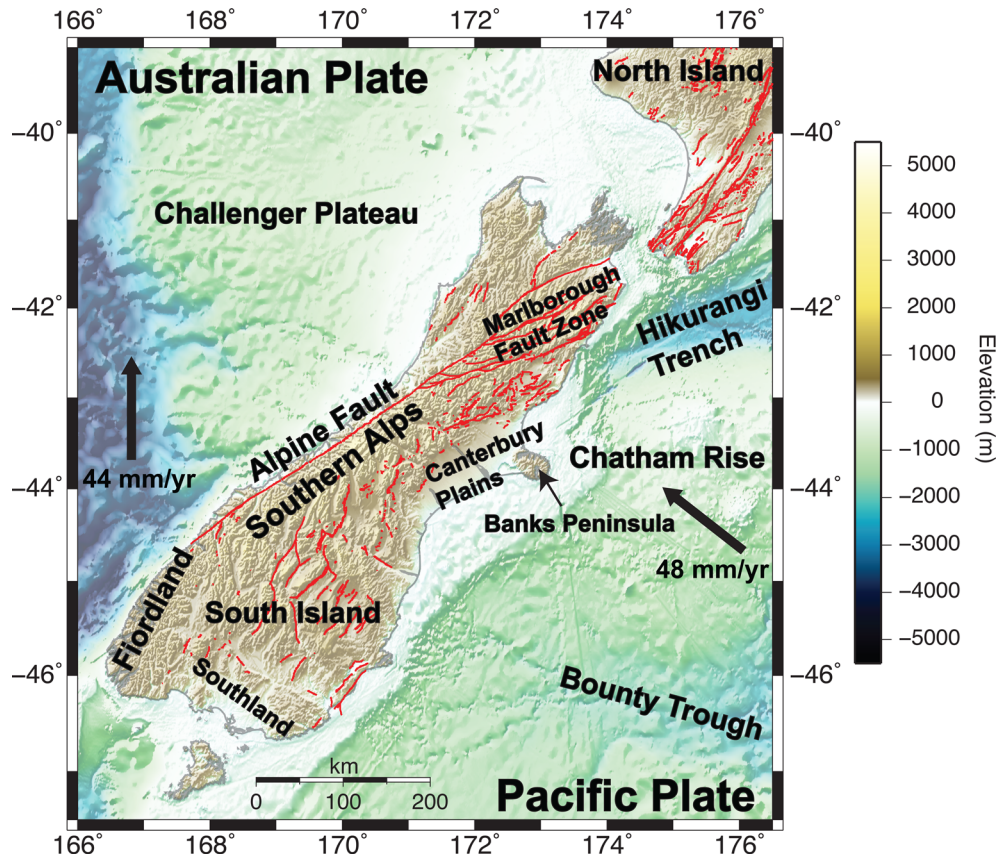* Now at: US Geological Survey, National Earthquake Information Center, Golden, CO 80225, USA.

Figure 1. Topography and bathymetry of the South Island of New Zealand and surrounding offshore regions. Major faults, including Alpine Fault, marked as red lines. Geographic and geological areas of interest labeled. Arrows show modern estimates of absolute plate motion of the Pacific and Australian plates in a hotspot reference frame (Gripp & Gordon 2002).

up to 50 km, more than 20 km deeper than its offshore flanks (van Avendonk *et al*. 2004; Scherwath *et al*. 2006; Bourguignon *et al*. 2007).

The anisotropic velocity structure of the South Island has been the focus of many studies. SKS shear wave splitting measurements on and offshore of New Zealand show a 100–200 km wide area of high anisotropy (1–2 s delay between fast and slow quasi-shear waves) surrounding and northwest of the Alpine Fault (Zietlow *et al*. 2014); fast directions in this region are largely subparallel (anticlockwise) to the strike of the Alpine Fault and suggest a wide shear zone along the plate boundary. Zietlow *et al*. (2014) argue that these observations best fit with models where: (1) deformation is distributed in the lithosphere or (2) deformation occurs discretely in the lithosphere and is distributed in the asthenosphere fanning out from the base of the lithosphere. Anisotropy observations of the upper mantle constrained from Pn arrival times (Collins & Molnar 2014) are consistent with SKS shear wave splitting measurements from Zietlow *et al*. (2014) and therefore suggest the 100–200 km wide band of deformation is present in the mantle lithosphere. Shear wave splitting measurements from local and regional earthquakes are also consistent with distributed deformation throughout the lithosphere (Karalliyadda & Savage 2013). Karalliyadda & Savage (2013) observe depth dependent and small-scale variations in shear wave splitting measurements, and suggest a complex pattern of deformation in the lithosphere beneath the South Island. Similarly, multiple phases of deformation resulting in destructive interference were suggested as a mechanism to explain low shear wave splitting measurements in the Southern Alps (Pulford *et al*. 2003). Teleseismic

receiver functions suggest anisotropy in the mid-crust below the Marlborough Fault Zone, although it was not possible to resolve its orientation (Wilson *et al*. 2004). Receiver functions in the northern South Island image a continuous and dipping Moho and show no evidence of faults piercing the Moho, and therefore suggest that variations in crustal thickness must be the result of distributed deformation of the lower crust (Wilson *et al*. 2004).

In this paper, we use ambient noise tomography (ANT) to investigate the isotropic and azimuthal anisotropic Rayleigh group velocity structure of the region surrounding the South Island. Isotropic velocity observations can corroborate crustal thickness observations to locate areas where the lower crust has undergone large-scale thickening. Azimuthal anisotropy observations at periods sensitive to the crust and upper mantle act as a proxy for the distribution of deformation and are sensitive to similar mechanisms that generate shear wave splitting observations from local earthquakes.

1.1 Rayleigh wave group velocity observations from ambient noise

Rayleigh wave group and phase velocity observations from ambient noise cross-correlations have been utilized in a wide variety of continental settings to gain insight into the crust and upper-mantle structure of the Earth (e.g. Yang *et al*. 2007, 2008; Stachnik *et al*. 2008; Yao *et al*. 2008; Zheng *et al*. 2008; Ritzwoller *et al*. 2011). While in rare cases offshore observations are possible from solely land-based stations (e.g. Zheng *et al*. 2011), in general, a
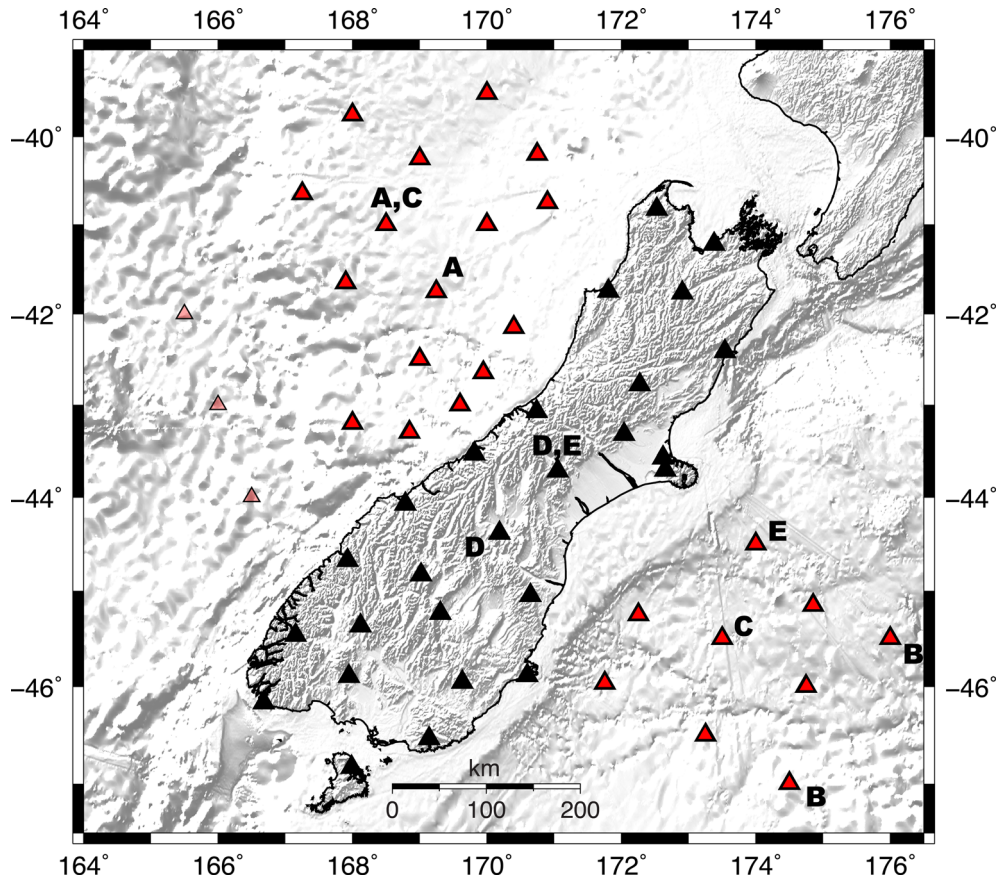
Figure 2. Stations used is this study including MOANA OBS seismic stations (red) and NZNSN land stations (black). MOANA stations with thin black borders and lighter colouring were included, but results were not used in tomography due to poor-quality stack cross-correlograms. Letters denote station pairs shown in Fig. 3 and correspond to the given Fig. 3 subplot label.

targeted offshore ocean bottom seismometer (OBS) deployment is required to make well-resolved offshore surface wave observations (e.g. Takeo *et al.* 2014; Zha *et al.* 2014; Ball *et al.* 2016a). Lin *et al.* (2007) previously utilized ANT with New Zealand land stations to constrain the 2-D Rayleigh wave group velocity of the North and South Island, and found that the narrow geometry of New Zealand and therefore narrow aperture of the array imposed limitations on their ability to constrain velocities at periods longer than 20–25 s. The linear geometry of New Zealand also limited their ability to investigate seismic structure offshore. The addition of offshore data allows us to investigate longer periods and therefore deeper velocity structure and allows us to better resolve the velocity structure on land due to a larger array aperture, higher ray density and better azimuthal coverage. Ball *et al.* (2016a) analysed surface waves from both onshore and offshore New Zealand to derive 1-D isotropic shear velocity models from isotropic Rayleigh and group and phase velocity tomograms. In this paper, we preform complementary anisotropic inversions to investigate anisotropy in Raleigh group velocity observations.

Recent studies have proven the efficacy of extracting azimuthal anisotropy information from the ambient noise field; the spatial resolution of these studies has improved the mapping of subsurface deformation of the lithosphere. Researchers have successfully implemented such methods to investigate tectonics in a variety of settings including the Alps (Fry *et al.* 2010), the Tehran Basin (Shirzad & Shomali 2014), near Canterbury, New Zealand (Fry

et al. 2014a) and using OBS data near the Shatsky Rise (Takeo *et al.* 2013).

2 DATA

We use continuous waveform data from 25 Marine Observations of Anisotropy Near Aotearoa (MOANA) broad-band OBS instruments and 26 coeval New Zealand National Seismic Network (NZNSN) land stations (Fig. 2). MOANA is an OBS experiment designed primarily to investigate the rheology and deformation of the lithosphere and mantle surrounding the Australian–Pacific plate boundary. MOANA deployed 30 OBS seismic stations for one year (network code ZU, 2009–2010 at IRIS DMC). All MOANA stations used in this study utilized Nanometrics Trillium 240 broad-band seismometers. Of these 30 stations deployed, 28 stations were successfully recovered. We exclude three OBS stations that lay on the deepest portion of our array due to poor quality of stacked cross-correlograms.

3 METHODS

3.1 Station pair cross-correlations for group velocity

We use a methodology similar to that outlined by Bensen *et al.* (2007) to compute the stacked cross-correlogram for a given
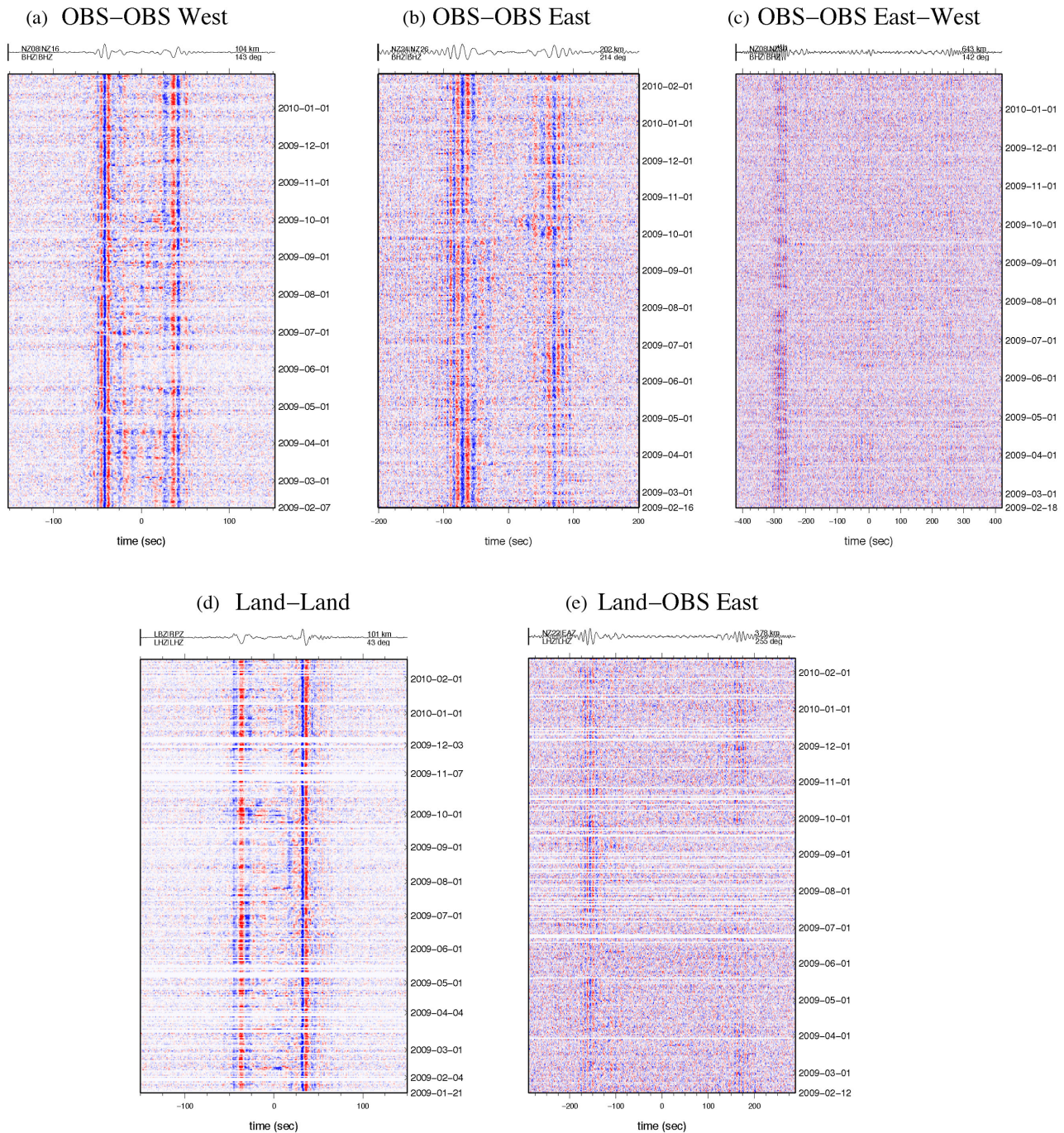
(a) OBS–OBS West (b) OBS–OBS East (c) OBS–OBS East–West

(d) Land–Land (e) Land–OBS East

Figure 3. Day stacks of hourly cross-correlation functions for sample pairs of MOANA and NZNSN stations plotted as a function of time. The top trace shows the total stack. Stations used are marked in Fig. 2. (a) Cross-correlation function for two OBS stations located to the west of the South Island. (b) Cross-correlation functions for two OBS stations located to the east of the South Island. (c) Cross-correlations for two OBS stations on either side of the South Island. (d) Cross-correlations for two land stations on the South Island. (e) Cross-correlation for land station and OBS station east of the South Island.

station pair. We use vertical component data from broad-band stations are downsampled to 1 sps. The use of data from only the vertical component helps isolate the Rayleigh wave signal. Prior to cross-correlation, we cut continuous data into 3600 s windows, remove instrument response, detrend, demean, bandpass filter from 2 to 100 s, and apply spectral whitening in the frequency domain. We cross-correlate all coeval data and stack all individual cross-correlations for the entire time period. In total, we obtain cross-correlations from 1275 station pairs. Examples of daily cross-correlations are shown

in Fig. 3 for different combinations of OBS stations and land-based stations. Cross-correlations between OBS stations located on the same side of the island (Figs 3a and b) show clear and symmetric Rayleigh wave packets for both the causal and acausal signal implying good azimuthal distribution of ambient noise sources. This is also true for cross-correlations between land stations (Fig. 3d). Cross-correlations are consistent over the duration of the experiment, encompassing a full year, indicating seasonal bias should be small. Cross-correlations between OBS stations on opposite sides

Table 1. Group velocity dispersion measurements removed by data culling criteria.

| Period (s)	Initial measurements	Removed due to low SNR (<10)	Removed due to outlier (>3 stds)	Removed due to close station proximity (>2 wavelengths)	Removed due to outlier (>2 stds) initial model	Remaining measurements	Average velocity (km s^{-1})
8	621	73	6	0	30	512 (83 per cent)	2.6
12	865	67	25	5	38	730 (84 per cent)	2.7
16	866	66	62	17	47	674 (78 per cent)	2.8
20	837	63	68	51	43	612 (73 per cent)	3.0
25	717	58	66	79	29	485 (68 per cent)	3.3
30	563	52	55	103	19	334 (60 per cent)	3.4
35	399	36	45	98	14	206 (52 per cent)	3.5
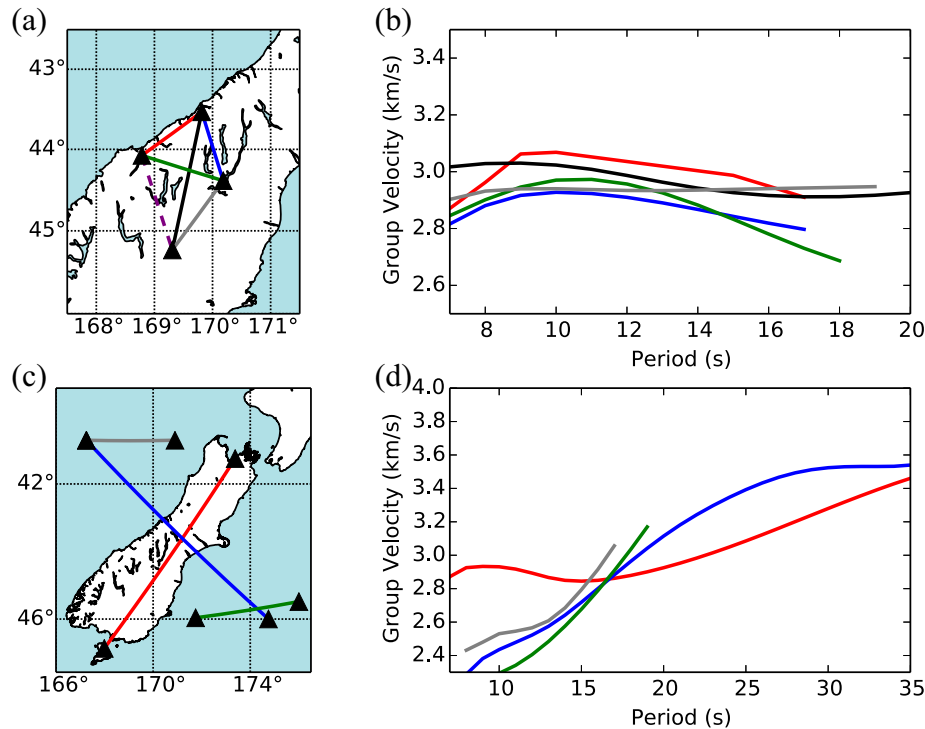
Figure 4. (a) and (b) Dispersion curves of group velocity for four closely spaced onshore stations near the Alpine Fault. Due to close station spacing, measurements at longer periods are not reliable and therefore not shown. Dashed purple line shows a station pair for which group velocity measurements were excluded due to poor quality. Fastest wave speeds are west of and parallel to the Alpine Fault (red curve) and slowest wave speeds are perpendicular to the Alpine Fault (blue curve). (c) and (d) Dispersion curves of Rayleigh group velocity for distant and offshore stations. Red curve is slow at longer periods due to thicker crust onshore. In contrast, slow wave speeds at short periods (blue curve) due to offshore sediments and water layer. Also shown are similarly oriented OBS station pairs on the Australian (grey) and Pacific plates (green).

of the island and those between land and OBS stations are less symmetric, yet still reveal good signal to noise and dispersive characteristics (Fig. 3c). The causal and acausal parts of the stacked cross-correlations are averaged prior to dispersion analysis for each station pair.

3.2 AFTAN

We use frequency–time analysis (FTAN) to extract period-dependent group velocity from a given station pair's stacked cross-correlogram (e.g. Bensen *et al.* 2007; Lin & Ritzwoller 2011; Ball *et al.* 2016a). We measure group velocity at periods of 8–35 s. We use the software package *aftan 1.1* (http://ciei.colorado.edu/Products/, last accessed 2014 May 19), an automated FTAN code developed by the University of Colorado's Center for Imaging the Earth's Interior. After extracting dispersion curves for individual station pairs,

we quality control data using multiple criteria (Table 1). Initially, we have ~400–800 measurements at a given period. The FTAN code will automatically remove data from discontinuous portions of the dispersion curve. We further cull measurements with a signal-to-noise ratio (SNR) less than 10, all measurements over three standard deviations from the mean, and all measurements where the station spacing is less than two wavelengths apart.

Possible evidence for anisotropy is apparent in dispersion curves alone (Fig. 4). In stations surrounding the Alpine Fault (Figs 4a and b), group velocity appears faster parallel and in close proximity to the Alpine Fault. At such small distances, long-period observations (>~18 s) are removed due to the two-wavelength cut-off. From such observations, it is difficult to determine if observed variations in dispersion observations are the result of isotropic or anisotropic velocity structure. At large station spacing (Figs 4c and d), which allows us to investigate long periods; broad regional velocity variations dominate our dispersion observations. Dispersion

measurements from distant station pairs show major geological regional differences including low-velocity offshore sediments at short periods (<15 s) and variations in crustal thickness at longer periods, with greatly thickened crust onshore near the plate boundary (Figs 4c and d). The difficulty in interpreting whether observed dispersion variations are the result of isotropic or anisotropic velocity structure demonstrates the benefit of performing tomographic inversions.

3.3 Group velocity tomography

After we cull station-pair dispersion observations, we perform tomographic inversions to create 2-D group velocity maps at selected periods. We use a damped least-squares approach, utilizing the code *tomo_sp_cu_s* (version 1.1, http://ciei.colorado.edu/Products/; last accessed 2014 May 19), developed by the University of Colorado's Center for Imaging the Earth's Interior (Barmin *et al.* 2001). Assuming a medium with a slight 2Ψ anisotropic component, group velocity can be written as a function of latitude, λ, longitude, ϕ, period, T, isotropic coefficient, A_0, anisotropic coefficient A_1 and A_2 and local ray direction, Ψ, in the form (Smith & Dahlen 1973):

$$c(\lambda, \phi, T, \Psi) = A_0(\lambda, \phi, T) + A_1(\lambda, \phi, T)\cos(2\Psi)$$
$$+ A_2(\lambda, \phi, T)\sin(2\Psi).$$

We perform tomographic inversions, individually, for both isotropic and isotropic + 2Ψ azimuthally anisotropic models for ambient noise measurements from 8 to 35 s periods. Isotropic models and the isotropic component of our anisotropic models are similar at periods up to 25 s. At longer periods, isotropic models, and the isotropic portion of our anisotropic model appear inconsistent. We find it likely this is a result of insufficient azimuthal coverage at longer periods to constrain the anisotropic component. We therefore restrict out anisotropic models to periods of 25 s or less. The percent anisotropy at a given node is defined as:

$$A_{\text{ani}} = \frac{\sqrt{A_1(\lambda, \phi, T)^2 + A_2(\lambda, \phi, T)^2}}{A_0(\lambda, \phi, T)}.$$

The *tomo_sp_cu_s* code is highly flexible and outputs a large quantity of information including information regarding ray density, resolution and azimuthal coverage at each node. This greatly aids in evaluating the robustness of the models to guide our interpretations. To further cull our data, we remove all dispersion measurements with misfit (s km^{-1}) greater than two standard deviations from the mean of our initial model and perform a second inversion to create our final models.

We use a node spacing of 0.5° for both isotropic and anisotropic components of our inversion. Traditional L-curve analysis (e.g. misfit versus smoothing parameter) was unsatisfactory due to the fact that model misfit remained relatively insensitive to smoothing coefficient changes. In order to better select our preferred smoothing coefficient, we utilize the sensitivity testing put forward by Ward *et al.* (2013). We extend the roughness metric of Ward *et al.* (2013) and examine the roughness of subsequent periods of investigation in A_{ani} and Ψ, assuming that satisfactorily smooth models will have minimized the relative variations between models at subsequent periods. Our models are most significantly controlled by α, a smoothing coefficient, and σ, the spatial smoothing length, which are inherently tied. In the models shown, we use 50 and 100 km for σ, and 250 and 500 for α for isotropic and anisotropic components of our models, respectively. We are able to use less smoothing for

the isotropic component of our model because, as this parameter is not dependent on path azimuth, it is better defined by our data and therefore requires less regularization. We find that anisotropy amplitude varies based on the smoothing selected, and we therefore avoid interpreting absolute anisotropy amplitudes; we instead focus on relative variations in amplitude and the direction of anisotropy, which appear stable regardless of the smoothing chosen.

Our models are well constrained due to our station density and array geometry. At short periods, up to ∼350 paths cross a single node in the centre of the array (Fig. S1, Supporting Information). At longer periods (35 s), the number of measurements is reduced by the constraints of minimum station spacing relative to wavelength. For example, at 35 s, ∼150 paths crossing a single node, roughly 40 per cent of the number of traces at 16 s (Fig. S1, Supporting Information).

We perform resolution analysis at each node, as described by Barmin *et al.* (2001), in which the resolution is the smallest distance in which two δ-like perturbations can be resolved. Realistically, the resolution cannot be smaller than 1°, twice the distance between two nodes. Therefore, we do not interpret features less than 1° × 1°. Our models have the highest resolution in the centre of our array, located at the central portion of the South Island (Fig. S2, Supporting Information). The resolution decreases towards the edges of our array. Our highest resolution is at the shortest periods. At 8 s, our isotropic model has a maximum resolution of ∼60 km. Resolution decreases at longer periods. The 35 s models have a best resolution of ∼80 km, increasing to 125 km around the edges of the array (Fig. S2, Supporting Information). We mask our models based on this resolution, only presenting regions where the resolution is estimated to be less than or equal to 200 km.

We investigated the inclusion of a 4Ψ anisotropic term in our models. We found that including 4Ψ anisotropy did not significantly reduce the misfit of our models (Fig. S3, Supporting Information). In models with the 4Ψ component, the amplitude of the 2Ψ term was on average 1.6–2.1 times larger than that of the 4Ψ term. In light of these observations, we chose not to present models including 4Ψ anisotropy and instead focus our interpretation on the more significant 2Ψ term. The observation that the 4Ψ component does not significantly improve model misfit is consistent with other Rayleigh wave anisotropy studies (e.g. Deschamps *et al.* 2008; Fry *et al.* 2010), although we note a pervious study on the South Island did included the 4Ψ anisotropy term (Fry *et al.* 2014a).

We use the bootstrap method to estimate the standard errors of our models (Fig. 5). This entailed randomly resampling with replacement the input data set of a given period and inverting to create 1000 unique models (e.g. Fig. S4 in the Supporting Information). The standard error of a given parameter was then calculated at each node.

4 RESULTS

We interpret 8, 12, 16, 20 and 25 s period anisotropic group velocity models (Figs 7 and 8). Due to the lack of azimuthal coverage, we only interpret isotropic group velocity models at 30 and 35 s period (Fig. 8). We evaluate sensitivity kernels for this range of periods given two distinct velocity models, one representing onshore South Island (thick continental crust) and one representing offshore Australian plate continental crust (Fig. 6) based on the 1-D velocity models from Van Avendonk *et al.* (2004). Offshore measurements are sensitive to greater depths due to the relatively thinner crust and therefore overall higher velocities and longer wavelengths. Our
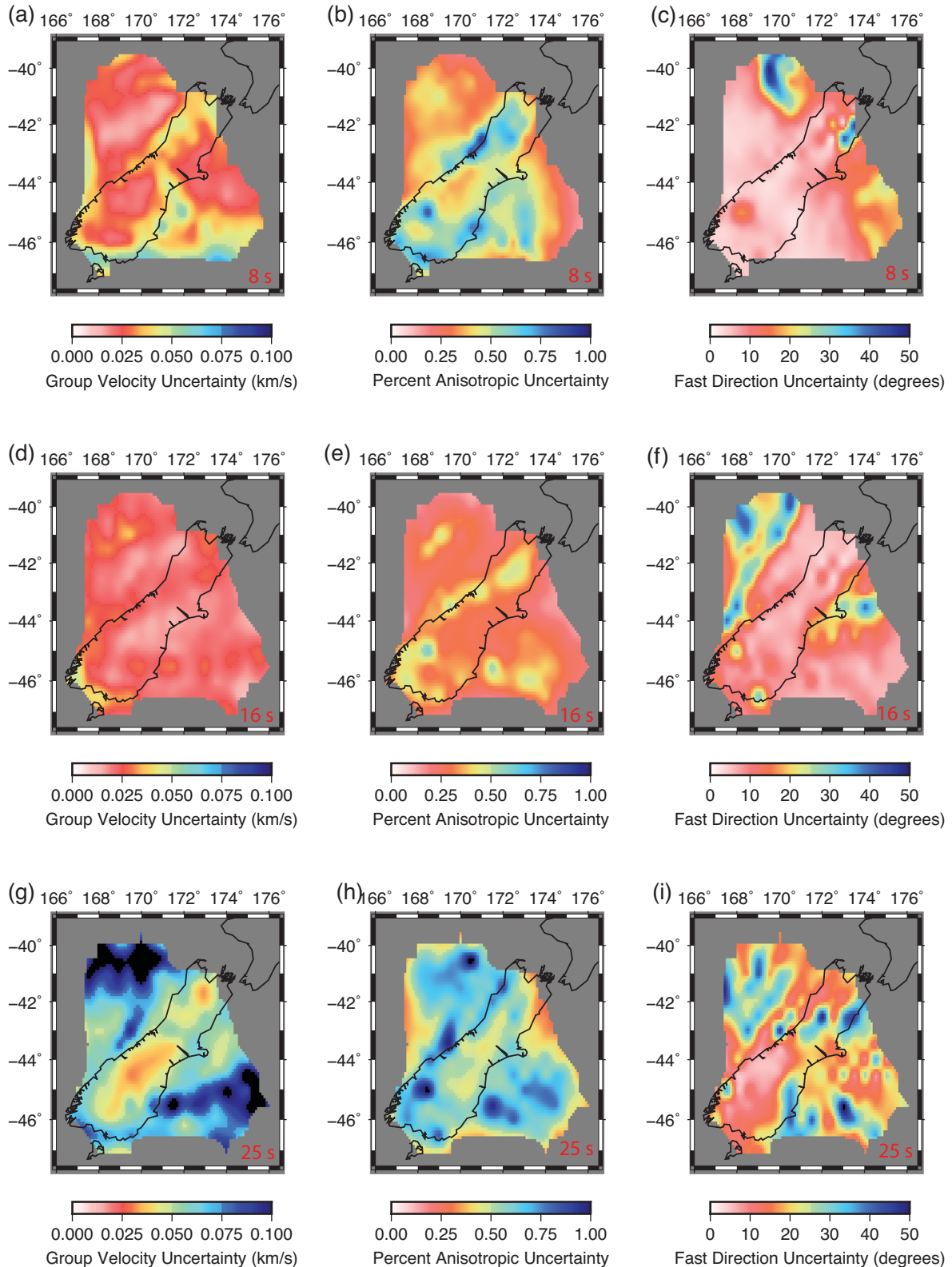
Figure 5. Bootstrap derived standard errors of model parameters for (a)–(c) 8 s period, (d)–(f) 16 s period and (g)–(i) 25 s period models. Fig. S4 in the Supporting Information shows an example of the distribution of the 1000 bootstrap samples at a single node in our model.

observations are sensitive from the shallow crust (8 s group measurements and peak sensitivity <10 km) to the mantle lithosphere (35 s group measurements and peak sensitivity ~45 km). At our shortest period observations (8 s, and to a lesser extent 12 s), the

water layer has a large effect on our offshore observations, as noted in previous offshore studies (e.g. Harmon *et al.* 2007).

In general, uncertainties increase with period due to the fact that there are fewer observation at longer periods. For the most
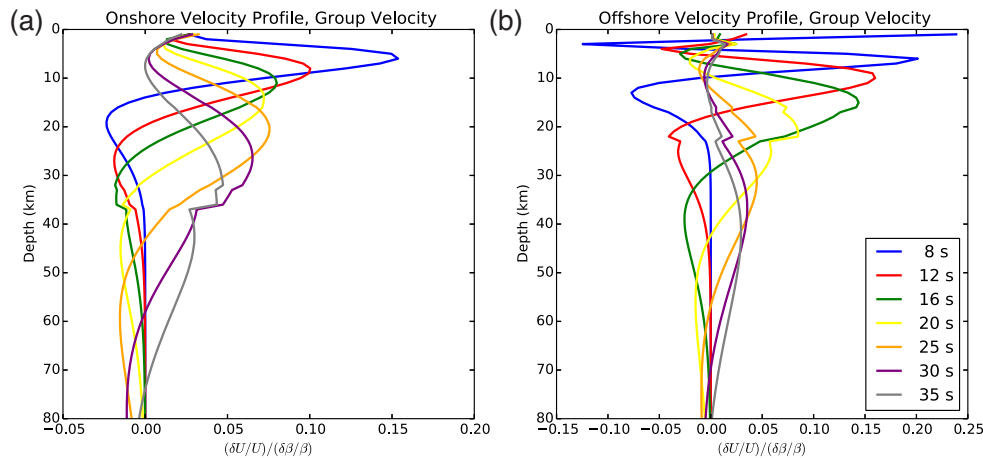
Figure 6. Depth sensitivity kernels for Rayleigh group velocity at periods used in this study. Kernels are calculated using two different velocity *P*-wave velocity profiles based on Van Avendonk *et al.* (2004), with assumed *Vp/Vs* ratio of 1.75 in the crust and 1.8 in the mantle. (a) Group velocity, sensitivity kernels for an onshore velocity profile with a thick crustal root. (b) Group velocity sensitivity kernels for offshore on the Australian plate.

part, the isotropic group velocity standard errors are small (<0.05 km s^{-1}), with the exception of near the edge of the array at longer periods (Fig. 5). 2Ψ fast directions are well constrained on the South Island (<15°), but uncertainties increase near the edge of the array and are high for some individual nodes (Fig. 5). The amplitude of anisotropy is well constrained at 16 s, but can be larger throughout the region at shorter and longer periods (Fig. 5). We note the uncertainties throughout when refereeing to specific interpretations that may be effected by poorly constrained regions of our models. Typically, uncertainties are relatively low on the South Island in the centre of the array.

4.1 8 and 12 s group velocity

At 8 and 12 s, group velocity is most sensitive to shear velocity in the upper crust (0–15 km for 8 s period and 0–20 km for 12 s period, Fig. 6) as well as to the compressional velocity in the water-layer offshore (e.g. Ball *et al.* 2016b). The contrast between low wave speed water-laden sediments versus higher wave speed crystalline basement is the largest signal at these periods. At 8 s, group velocity is higher onshore (up to 3.0 km s^{-1}) than offshore (as low as 1.9 km s^{-1}) (Fig. 7a). Offshore of the Pacific plate has especially low velocities as compared to the Australian plate at both 8 and 12 s periods (Figs 7a and c), with the lowest group velocities where sediment is thickest (Fig. 9a). Low velocities that edge into the Canterbury Plains are likely due to the presence of young sedimentary and volcanic rock (Grindley *et al.* 1959), and agree with previous surface wave observations (Lin *et al.* 2007) and shallow shear velocity observations (Fry *et al.* 2014b). At 8 s, our shallowest observations, the south-central portion of the Southern Alps is seismically fast as compared to the surrounding basement rock. At 12 s, fast wave speeds are also observed beneath the Southern Alps, as well as in Fiordland.

At 8 s, azimuthal anisotropy fast directions are slightly subparallel (anticlockwise) to the Alpine Fault on land, and reduce in amplitude out to the flanks (Fig. 7b). In the southern portion of the island, fast directions rotate slightly anticlockwise as compared to the north. The relative amplitude of anisotropy is much higher at 8 s as compared other periods, with a maximum of 6 per cent anisotropy in the central portion of the island, spatially coinciding with modern day estimations of maximum shear strain rate (Beavan & Haines 2001).

At 12 s, Alpine Fault parallel fast directions are largely isolated to the South Island, while offshore fast directions trend northwest–southeast (Fig. 7d). The same anticlockwise rotation in the southern portion of the island is observed as at 8 s. In the Canterbury region, our 8 s fast direction trends northeast–southwest, while group velocity measurements using only land stations (Fry *et al.* 2014a), have east–west trending fast directions here. This may be due to parametrization variations between the two models (e.g. node spacing and regularization choices), or may be a result of differences in array geometry and data availability (i.e. the more complete azimuthal coverage in this study). It is possible that, as a result of the scale of our study region and resultant model parametrization, our models present broader regionally averaged velocities. Fast directions are more consistent between the two models at longer periods (15 s versus 16 s). The amplitude of anisotropy varies between the two models, but as we noted previously, this amplitude is highly dependent on the regularization parameters chosen (Fig. S5, Supporting Information). At 12 s, our model shows a northeast–southwest trending fast direction in this region. In contrast, local shear wave splitting results indicate fast axis northwest–southeast that is consistent with SHmax, and perhaps indicative of shallower upper crustal sampling of the local shear wave splitting (Holt *et al.* 2013).

4.2 16 and 20 s group velocity

From periods of 16 to 20 s, group velocity has a peak sensitivity to shear velocity at depths from 15 to 22 km offshore (Fig. 6), and therefore this period range is sensitive to the transition from the crust to the mantle. Assuming a thickened crust velocity profile on land (Fig. 6), group velocity is largely sensitive to the mid-crust (10–14 km). At 16 s, the velocity distinction between offshore and onshore regions does not appear to relate to either the presence of sediment or closely to changes in crustal thickness (Fig. 7e). High velocities are apparent in Fiordland, as with shorter periods. A low-velocity anomaly surrounds Canterbury as compared to the rest of the island. Low group velocities at 18 s in the Canterbury region were observed in previous studies (Lin *et al.* 2007), but the offshore geometry of this feature could not be observed using solely land stations. At 20 s, the South Island has lower velocities than its offshore flanks (Fig. 8a), with group velocities approaching 3.4 km s^{-1} offshore as compared to 2.75 km s^{-1} observed
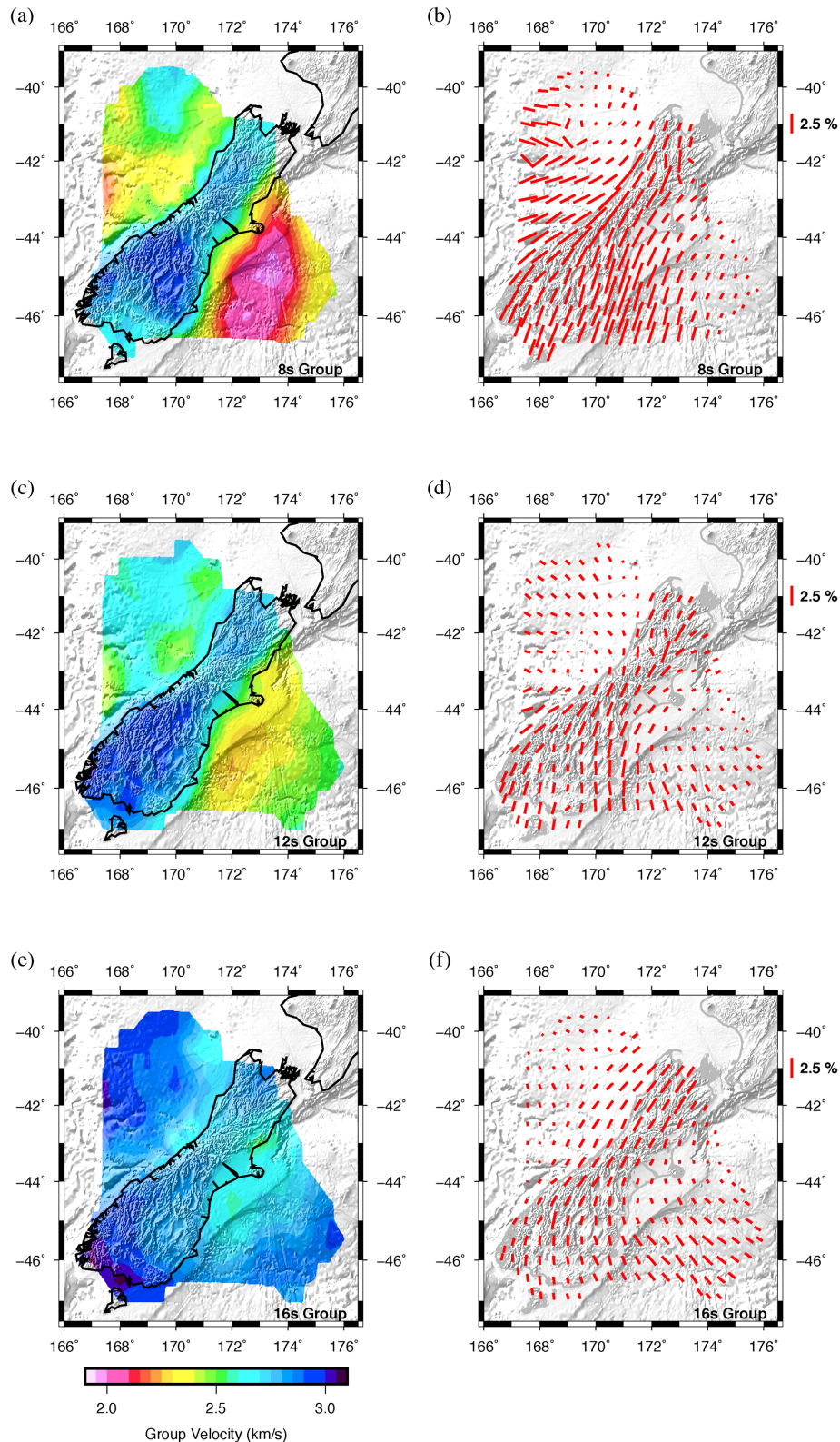
Figure 7. Anisotropic group velocity models 8, 12 and 16 s periods. (a), (c) and (e) The isotropic component of the group velocity model is shown on the left and (b), (d) and (f) the anisotropic component on the right.

on land. This variation is likely the result of thickened crust under the South Island (Fig. 9b). The exception to this is the Fiordland and Southland regions, where velocities remain relatively high even though crust is especially thick (Salmon *et al.* 2013). This is

consistent with constraints from local earthquake tomography that show Fiordland contains regions of high *P*-wave velocities throughout the crust, primarily associated with surface exposures of the Western Fiordland Orthogneiss (Eberhart-Phillips & Reyners 2001),
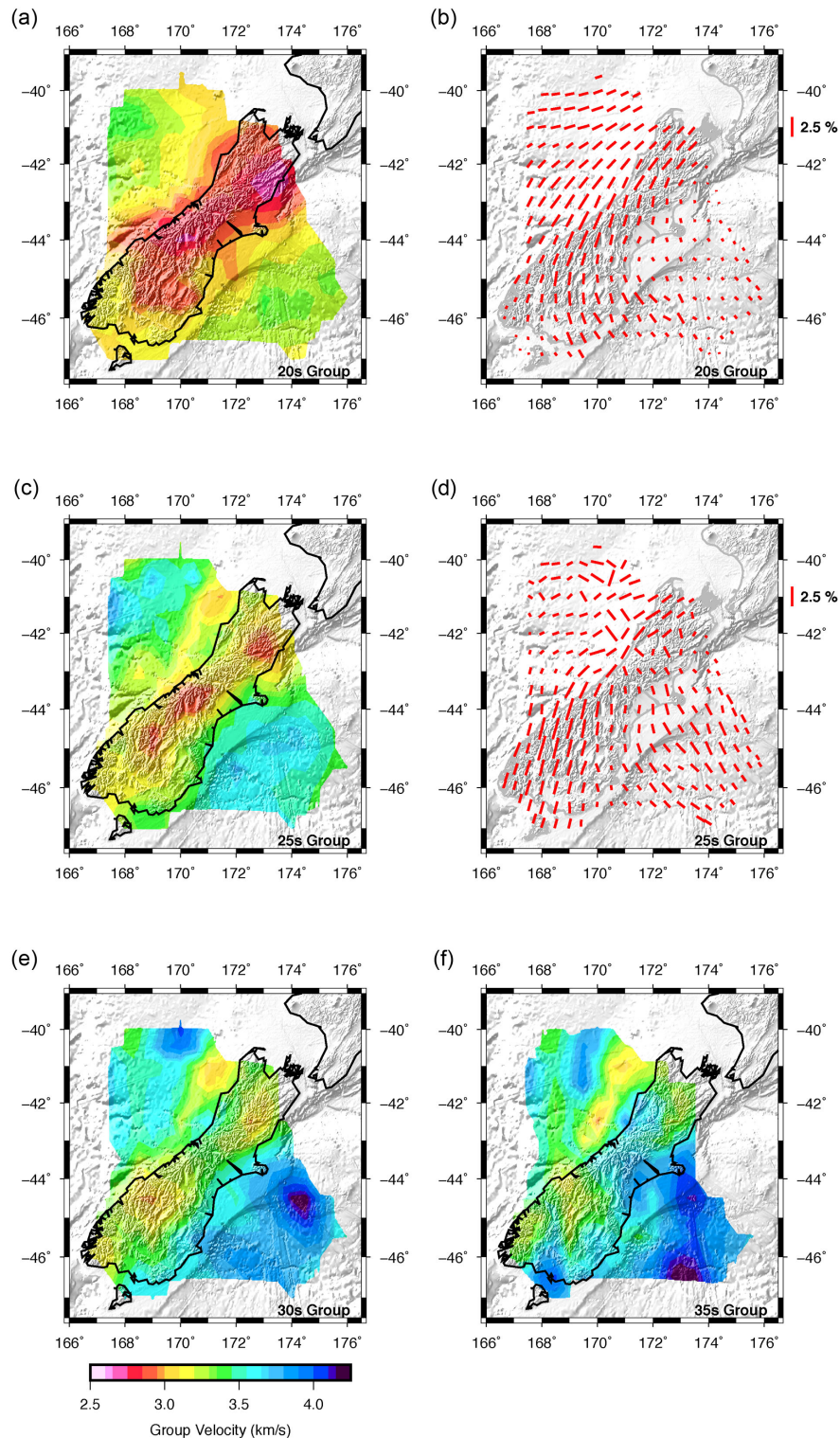
Figure 8. Anisotropic group velocity models (a) and (b) 20 and (c) and (d) 25 s periods and isotropic models for (e) 30 and (f) 35 s periods. (e) and (f) The low-velocity anomaly on the offshore on the Australian plate (41 N 171 E) at long periods is likely and artefact of our inversion.

although our observations suggest a broader region of high-velocity crust.

At periods of 16 and 20 s, azimuthal anisotropy fast directions are similar. Fast directions appear subparallel (anticlockwise) to the strike of the Alpine Fault, and continue to rotate anticlockwise in the southern portion of the island. Unlike the 12 s observations,

Alpine Fault subparallel fast directions continue ~200 km offshore northeast of the island. Further offshore on the Australian plate, fast directions rotate to east–west, although the fast directions are poorly constrained in this region (Fig. 5). On the Pacific plate, where uncertainties are smaller, fast directions rotate to point northwest–southeast, nearly parallel to absolute plate motion (Fig. 1).
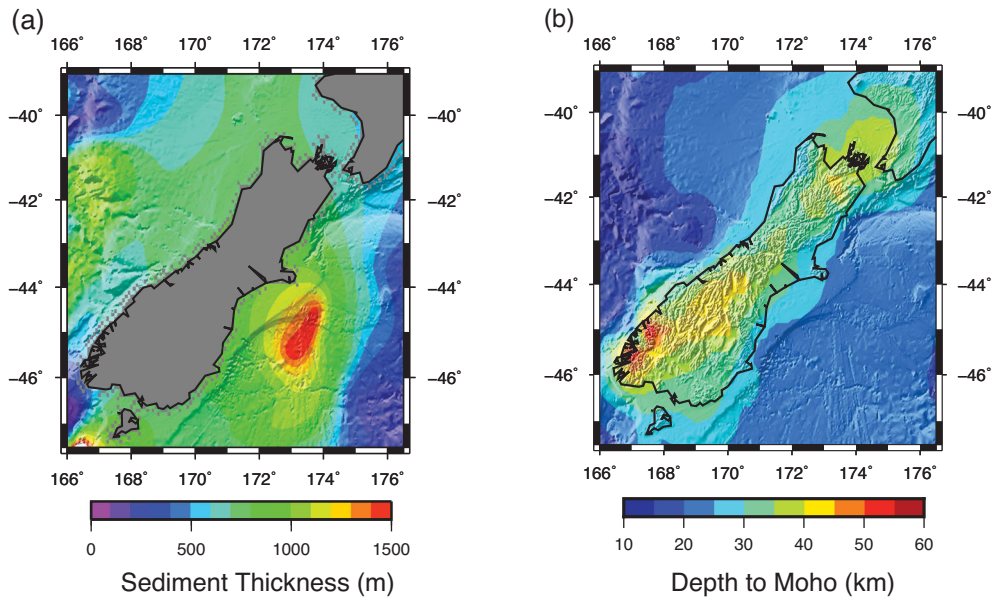
Figure 9. (a) Offshore sediment thickness from Divins (2003). (b) Moho depth below sea level from Salmon *et al.* (2013).

4.3 25, 30 and 35 s group velocity

At 25 and 30 s, group velocities are lower beneath the South Island, particularly beneath the Southern Alps (Figs 8c and e), likely the result of thickened crust beneath the South Island. At 35 s, velocities in the South Island are comparable to those offshore and slowest in the southern and northern portions of the Island where the crust is thickest (Fig. 8f). A notable low-velocity anomaly appears offshore to the northwest of the island, present in 25, 30 and 35 s maps (Figs 8c, e and f). While this feature is well defined at a range of periods, it is likely an artefact as it lies on the edge of our array, the uncertainties in this region are relatively high at these periods (25 s+) (Fig. 5), it is near the size of our resolution at these periods, and there is not a clear geological explanation for this discrete low-velocity zone in the Challenger Plateau. As well, previously derived isotropic phase-velocity tomograms presented by Ball *et al.* (2016a) derived from both ambient noise and earthquake data did not image a similar feature. At 25 s, anisotropic observations are similar to those at 20 s, but show more complexity. This complexity is likely due to the reduced azimuthal coverage as a result of less useable observations, and therefore associated uncertainties (Fig. 5).

5 GEOLOGICAL INTERPRETATIONS

Major regional variations in isotropic Rayleigh wave group velocity are attributed to either low wave speed water-laden sediment or large-scale variations in crustal thickness. At short periods (8, 12 s), we observe that the offshore region both east and west of the South Island has low velocities relative to onshore (1.75 km s^{-1} offshore versus 3.0 km s^{-1} onshore for 8 s group velocity). Areas with especially low group velocity correlate with areas of increased sediment thickness (Fig. 9a; Divins 2003). At longer periods (16+s), low velocities in the South Island are the result of thickened crust (Fig. 9b). Offshore in regions of thinner crust, high velocities are the result of mantle sensitivity of long-period surface waves. While these observations dominate our models, there are a variety of other important observations of geological interest.

5.1 Anisotropy observations

Anisotropy in the crust is commonly attributed to cracks or mineral alignment (Rabbel & Mooney 1996). Anisotropy as a result of aligned fluid filled cracks is expected to have fast directions subparallel to the maximum local compressive stress orientation (Crampin 1994). The observed maximum horizontal stress near the Alpine Fault, determined from focal mechanisms from shallow (<~15 km) microseismicity, is roughly 115° (Boese *et al.* 2012), nearly perpendicular to our observed azimuthal fast directions near the fault. Therefore, it is unlikely that the anisotropy that we observe near the Alpine Fault is due to aligned crustal cracks. Our shortest period group velocity measurements (8 s) are sensitive to depths from approximately 0–20, with peak sensitivity at approximately 8 km depth. Given the integrative nature of surface waves, there may be crack-induced anisotropy in the upper few kilometres of the crust that our results cannot resolve. In terms of mineral alignment, rock samples from the Alpine Fault mylonites and the Haast Schist terrane are highly anisotropic, with *P*-wave anisotropy reaching 17 per cent at pressures correlating to the mid-crust (Okaya *et al.* 1995). Anisotropy increases with metamorphic grade, and therefore the magnitude of anisotropy increases toward the Alpine Fault (Okaya *et al.* 1995). These anisotropic basement terranes are dramatically sheared along the Alpine Fault (Fig. 10). Regional body wave derived tomograms of the South Island image uniform *P*-wave velocities to 20 km depth suggesting that basement terranes observed on the surface may extend into the mid-crust (Eberhart-Phillips & Bannister 2002). East of the South Island, seismic reflection data suggests that the Otago Schist terrane extends though most of the crust (Mortimer *et al.* 2002). Our azimuthal anisotropy fast directions follow the bend in basement terranes (Fig. 10), most distinctly in our group velocity models at 12, 16 and 20 s periods (Figs 7d, f and 8b), suggesting that azimuthal anisotropy here is the result of fabrics generated from the dextral shearing of crustal rocks along the Alpine Fault. Group velocity models at 8 s show a similar pattern but the counterclockwise rotation of fast directions in the southeast is less distinct. 8–20 s group velocities onshore are most sensitive to the upper to mid-crust (<20 km) (Fig. 6),
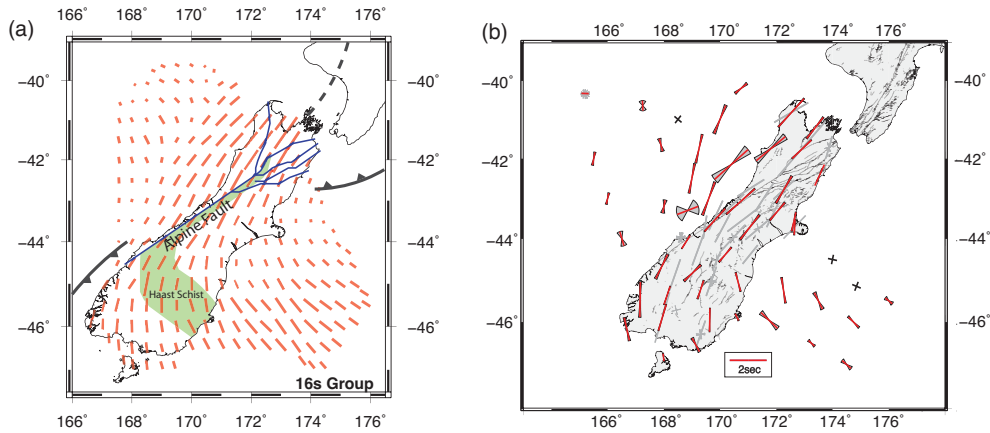
Figure 10. (a) Azimuthal fast direction of 16 s group velocity model compared to distinct dextral shearing of basement terranes (Haast Schist terrane). (b) SKS shear wave splitting measurements made by Zietlow *et al.* (2014) (red bars). Previous SKS shear wave splitting measurements from Klosko *et al.* (1999) and Duclos *et al.* (2005) plotted as light grey lines. Black crosses show null measurements.

and therefore the foliated basement terranes. Offshore, our longest period robust azimuthal anisotropy observations (20 s) are likely sensitive to a depth near the Moho. This suggests sensitivity to anisotropic olivine, which is often interpreted to be the dominant source of anisotropy in the mantle (e.g. Silver & Chan 1991). We note that the associated uncertainties are larger at these longer periods, but still uncertainties are relatively low on most of the South Island. In general, the orientation of anisotropic fast directions close to the Alpine Fault is rotated anticlockwise from the strike of the fault.

The amplitude of anisotropy, ~2.5 per cent, appears consistent throughout the South Island in both the 16 and 20 s models, however, we note that magnitude of anisotropy is dependent on the smoothness chosen for the inversion, ranging from ~2 to 6 per cent at these periods (see Fig. S5 in the Supporting Information for more details). In the models we present, the standard errors associated with the amplitude of anisotropy at these periods is relatively low (<.5 per cent). The amount of anticlockwise rotation from the Alpine Fault is ~10°–30° in the 16 and 20 s models, higher than at 8 and 12 s, and is more diffuse. Our group velocity fast directions correlate well with previous SKS shear wave splitting measurements (Klosko *et al.* 1999; Duclos *et al.* 2005; Zietlow *et al.* 2014) (Fig. 10), and Pn anisotropy observations (Collins & Molnar 2014), suggesting consistent deformation throughout the mid-lower crust and mantle lithosphere. Our observations show less complexity in anisotropy fast directions than that observed by local and regional earthquake shear wave splitting (Karalliyadda & Savage 2013; Karalliyadda *et al.* 2015), some of which may be attributed to differing resolution and depth sampling between methods. The smoothness of our group velocity models is likely a result of the broad sensitivity of surface waves and the smoothing applied in our tomography. The lack of azimuthal coverage at long periods (>20 s) reduces our ability to reliably investigate anisotropy of the lower crust on the South Island.

The observed anticlockwise rotation east of the Alpine Fault agrees with predicted finite strain ellipses from models presented by Little *et al.* (2002). These models predict decreasing horizontal strain away from the Alpine Fault, with minimal strain on the eastern portion of the island. We also observe a decrease in the magnitude of anisotropy laterally away from the Alpine Fault, though more broadly distributed, similar to what Little *et al.* (2002) noted to be the case with fast polarization directions of SKS.

5.2 Offshore Pacific and Australian plates

In nearly all of our anisotropic inversions, Rayleigh wave group velocity fast directions offshore on the Pacific plate align northwest–southeast, parallel to absolute plate motion of the Pacific plate (Gripp & Gordon 2002). The exception is the 8 s period model that suggests that anisotropic fabric is not present in shallow sediment (Fig. 7b). For the most part, the standard errors associated with the direction on anisotropy are low (<15°) on the Pacific plate (Fig. 5). Fast direction orientations far (>150 km) offshore on the Australian plate do not align with absolute plate motion (north–south). In this region, our observations are inconsistent at different periods and the associated uncertainties are the highest (Fig. 5). We therefore do not interpret the complex and varying pattern of anisotropy on the Australian plate as significant. Closer to shore, our fast directions align with the Alpine Fault.

5.3 Width of deformation along the South Island

Determining the precise width of upper crustal deformation due to the transform plate boundary using group velocity models is difficult. Limitations arise due to the horizontal sensitivity of surface waves, our model parametrization (e.g. node spacing), and the effect of our regularization parameters. In many of our models, Rayleigh wave group velocity fast directions change orientation between adjacent nodes by ~90°, suggesting that our smoothing is sufficiently small that our node spacing (0.5°) primarily controls the resolution of our fast direction observations.

Determining the exact depth extent of anisotropy and therefore the implied crustal deformation is difficult due to the broad and overlapping depth sensitivity kernels of Rayleigh wave group velocity observations (Fig. 6). While observations at specific periods have peak sensitivities at specific depths, they can still be sensitive to tens of kilometres of the crust (Fig. 6). Still, the sensitivity kernels at 8 and 20 s are relatively distinct, yet they show a consistent pattern of anisotropy. This suggests that deformation is distributed over a wide band throughout the upper crust of the South Island that extends into the mid-crust. The predominantly long wavelengths of Rayleigh waves used to derive these maps makes it unlikely that the distribution of anisotropy we observe is affected by small-scale deformation, such as localized shear surrounding the Alpine Fault (e.g. Norris & Toy 2014). The fact that we observe consistent bands

of anisotropy both offshore to the east, and to the west of the Alpine Fault, and that this anisotropy turns with mapped metamorphic terranes, points to our observations being the result of broad crustal deformation.

Consistent observations onshore of the South Island and off the west coast, where thinner crust causes surface waves to be sensitive to the mantle, suggests that the pattern of deformation extends into the mantle, consistent with previous deep observations (e.g. Zietlow *et al.* 2014). These combined observations suggest deformation is distributed vertically throughout the whole lithosphere.

6 CONCLUSIONS

We present regional scale observations of group velocity both on- and offshore of the South Island of New Zealand. Using observations from ambient noise, we create group velocity models from 8 to 35 s, with anisotropic observations up to 25 s, sensitive to a depth range from the upper crust to the upper mantle. We find that at short periods (8–12 s), the influence of the water layer and the contrast between water-laden sediments offshore and basement rock on land dominates our isotropic group velocity observations. The thickened crust under the South Island is imaged by low group velocities at longer periods (16–30 s). Group velocity azimuthal fast directions correlate well with the dextral shear in basement terranes along the Alpine Fault. Anisotropy fast directions at depths sensitive to the crust do not align with maximum horizontal fast directions and therefore appear to be the result of rock fabric as opposed to the preferred alignment of cracks. Fast directions offshore on the Pacific plate are parallel with absolute plate motion. Our observations correlate well with previously observed SKS and Pn anisotropy fast directions, and we therefore suggest that the pattern of distributed deformation in the crust appears to be largely consistent throughout the lithosphere.

REFERENCES

Ball, J.S., Godin, O.A., Evers, L.G. & Cheng, L., 2016a. Long-range correlations of microseism-band pressure fluctuations in the ocean, *Geophys. J. Int.,* **206**(2), 825–834.

Ball, J.S., Sheehan, A.F., Stachnik, J.C., Lin, F.-C., Yeck, W.L. & Collins, J.A., 2016b. Lithospheric shear velocity structure of South Island, New Zealand, from amphibious Rayleigh wave tomography, *J. geophys. Res.,* **121**, 3686–3702.

Barmin, M., Ritzwoller, M.H. & Levshin, A., 2001. A fast and reliable method for surface wave tomography, *Pure appl. Geophys.,* **158**, 1351–1375.

Beavan, J. & Haines, J., 2001. Contemporary horizontal velocity and strain rate fields of the Pacific-Australian plate boundary zone through New Zealand, *J. geophys. Res.,* **106**(B1), 741, doi:10.1029/2000JB900302.

Bensen, G.D., Ritzwoller, M.H., Barmin, M.P., Levshin, A.L., Lin, F., Moschetti, M.P., Shapiro, N.M. & Yang, Y., 2007. Processing seismic ambient noise data to obtain reliable broad-band surface wave dispersion measurements, *Geophys. J. Int.,* **169**(3), 1239–1260.

Boese, C.M., Townend, J., Smith, E. & Stern, T., 2012. Microseismicity and stress in the vicinity of the Alpine Fault, central Southern Alps, New Zealand, *J. geophys. Res.,* **117**, B02302, doi:10.1029/2011JB008460.

Bourguignon, S., Stern, T.A. & Savage, M.K., 2007. Crust and mantle thickening beneath the southern portion of the Southern Alps, New Zealand, *Geophys. J. Int.,* **168**, 681–690.

Collins, J.A. & Molnar, P., 2014. Pn anisotropy beneath the South Island of New Zealand and implications for distributed deformation in continental lithosphere, *J. geophys. Res.,* **119**, 7745–7767.

Crampin, S., 1994. The fracture criticality of crustal rocks, *Geophys. J. Int.,* **118**, 428–438.

Deschamps, F., Lebedev, S., Meier, T. & Trampert, J., 2008. Azimuthal anisotropy of Rayleigh-wave phase velocities in the east-central United States, *Geophys. J. Int.,* **173**, 827–843.

Divins, D.L., 2003. *Total Sediment Thickness of the World's Oceans and Marginal Seas,* NOAA National Geophysical Data Center, Boulder, CO.

Duclos, M., Savage, M.K., Tommasi, A. & Gledhill, K.R., 2005. Mantle tectonics beneath New Zealand inferred from SKS splitting and petrophysics, *Geophys. J. Int.,* **163**, 760–774.

Eberhart-Phillips, D. & Bannister, S., 2002. Three-dimensional crustal structure in the Southern Alps region of New Zealand from inversion of local earthquake and active source data, *J. geophys. Res.,* **107**(B10), 2262, doi:10.1029/2001JB000567.

Eberhart-Phillips, D. & Reyners, M., 2001. A complex, young subduction zone imaged by three-dimensional seismic velocity, Fiordland, New Zealand, *Geophys. J. Int.,* **146**, 731–746.

Fry, B., Deschamps, F., Kissling, E., Stehly, L. & Giardini, D., 2010. Layered azimuthal anisotropy of Rayleigh wave phase velocities in the European Alpine lithosphere inferred from ambient noise, *Earth planet. Sci. Lett.,* **297**, 95–102.

Fry, B., Davey, F., Eberhart-Phillips, D. & Lebedev, S., 2014a. Depth variable crustal anisotropy, patterns of crustal weakness, and destructive earthquakes in Canterbury, New Zealand, *Earth planet. Sci. Lett.,* **392**, 50–57.

Fry, B., Eberhart-Phillips, D. & Davey, F., 2014b. Mantle accommodation of lithospheric shortening as seen by combined surface wave and teleseismic imaging in the South Island, New Zealand, *Geophys. J. Int.,* **199**, 499–513.

Grindley, G.W., Harrington, H.J. & Wood, B.L.W., 1959. The geological map of New Zealand 1: 2 000 000, N.Z. Geological Survey Bulletin No. 66. New Zealand Department of Scientific and Industrial Research, Wellington, New Zealand.

Gripp, A.E. & Gordon, R.G., 2002. Young tracks of hotspots and current plate velocities, *Geophys. J. Int.,* **150**, 321–361.

Harmon, N., Forsyth, D. & Webb, S., 2007. Using ambient seismic noise to determine short-period phase velocities and shallow shear velocities in young oceanic lithosphere, *Bull. seism. Soc. Am.,* **97**, 2009–2023.

Holt, R.A., Savage, M.K., Townend, J., Syracuse, E.M. & Thurber, C.J., 2013. Crustal stress and fault strength in the Canterbury Plains, *Earth planet. Sci. Lett.,* **383**, 173–181.

Houlié, N. & Stern, T., 2012. A comparison of GPS solutions for strain and SKS fast directions: implications for modes of shear in the mantle of a plate boundary zone, *Earth planet. Sci. Lett.,* **345–348**, 117–125.

Karalliyadda, S.C. & Savage, M.K., 2013. Seismic anisotropy and lithospheric deformation of the plate-boundary zone in South Island,

New Zealand: inferences from local *S*-wave splitting, *Geophys. J. Int.,* **193,** 507–530.

Karalliyadda, S.C., Savage, M.K., Sheehan, A.F., Collins, J., Zietlow, D. & Shelley, A., 2015. *S*-wave splitting in the offshore South Island, New Zealand: insights into plate-boundary deformation, *Geochem. Geophys. Geosyst.,* **16,** 2829–2847.

Klosko, E.R., Wu, F.T., Anderson, H.J., Eberhart-Phillips, D., McEvilly, T.V., Audoine, E., Savage, M.K. & Gledhill, K.R., 1999. Upper mantle anisotropy in the New Zealand Region, *Geophys. Res. Lett.,* **26,** 1497–1500.

Lin, F.C. & Ritzwoller, M.H., 2011. Helmholtz surface wave tomography for isotropic and azimuthally anisotropic structure, *Geophys. J. Int.,* **186,** 1104–1120.

Lin, F.C., Ritzwoller, M.H., Townend, J., Bannister, S. & Savage, M.K., 2007. Ambient noise Rayleigh wave tomography of New Zealand, *Geophys. J. Int.,* **170,** 649–666.

Little, T.A., Savage, M.K. & Tikoff, B., 2002. Relationship between crustal finite strain and seismic anisotropy in the mantle, Pacific-Australia plate boundary zone, South Island, New Zealand, *Geophys. J. Int.,* **151,** 106–116.

Mortimer, N., Davey, F.J., Melhuish, A., Yu, J. & Godfrey, N.J., 2002. Geological interpretation of a deep seismic reflection profile across the Eastern Province and Median Batholith, New Zealand: crustal architecture of an extended Phanerozoic convergent orogen, *New Zeal. J. Geol. Geophys.,* **45**(September), 349–363.

Norris, R.J. & Cooper, A.F., 2001. Late Quaternary slip rates and slip partitioning on the Alpine Fault, New Zealand, *J. Struct. Geol.,* **23**(2), 507–520.

Norris, R.J. & Toy, V.G., 2014. Continental transforms: a view from the Alpine Fault, *J. Struct. Geol.,* **64,** 3–31.

Okaya, D., Christensen, N., Stanley, D. & Stern, T., 1995. Crustal anisotropy in the vicinity of the Alpine Fault Zone, South Island, New Zealand, *New Zeal. J. Geol. Geophys.,* **38**(4), 579–583.

Pulford, A., Savage, M.K. & Stern, T., 2003. Absent anisotropy: the paradox of the Southern Alps orogen, *Geophys. Res. Lett.,* **30**(20), 1–4.

Rabbel, W. & Mooney, W.D., 1996. Seismic anisotropy of the crystalline crust: what does it tell us?, *Terra Nova,* **8,** 16–21.

Ritzwoller, M.H., Lin, F.-C. & Shen, W., 2011. Ambient noise tomography with a large seismic array, *C. R. Geosci.,* **343**(8–9), 558–570.

Salmon, M., Kennett, B.L.N., Stern, T. & Aitken, A.R., 2013. The Moho in Australia and New Zealand, *Tectonophysics,* **609,** 288–298.

Scherwath, M., Stern, T., Davey, F. & Davies, R., 2006. Three-dimensional lithospheric deformation and gravity anomalies associated with oblique continental collision in South Island, New Zealand, *Geophys. J. Int.,* **167**(2), 906–916.

Shirzad, T. & Shomali, Z.H., 2014. Shallow crustal radial anisotropy beneath the Tehran basin of Iran from seismic ambient noise tomography, *Phys. Earth planet. Inter.,* **231,** 16–29.

Silver, P.G. & Chan, W.W., 1991. Shear wave splitting and subcontinental mantle deformation, *J. geophys. Res.,* **96**(B10), 16 429–16 454.

Smith, M.L. & Dahlen, F.A., 1973. The azimuthal dependence of Love and Rayleigh wave propagation in a slightly anisotropic medium, *J. geophys. Res.,* **78**(17), 3321, doi:10.1029/JB078i017p03321.

Stachnik, J.C., Dueker, K., Schutt, D.L. & Yuan, H., 2008. Imaging Yellowstone plume-lithosphere interactions from inversion of ballistic and diffusive Rayleigh wave dispersion and crustal thickness data, *Geochem. Geophys. Geosyst.,* **9**(6), doi:10.1029/2008GC001992.

Sutherland, R., Davey, F. & Beavan, J., 2000. Plate boundary deformation in South Island, New Zealand, is related to inherited lithospheric structure, *Earth planet. Sci. Lett.,* **177,** 141–151.

Takeo, A., Forsyth, D.W., Weeraratne, D.S. & Nishida, K., 2014. Estimation of azimuthal anisotropy in the NW Pacific from seismic ambient noise in seafloor records, *Geophys. J. Int.,* **199**(1), 11–22.

Takeo, A., Nishida, K., Isse, T., Kawakatsu, H., Shiobara, H., Sugioka, H. & Kanazawa, T., 2013. Radially anisotropic structure beneath the Shikoku Basin from broadband surface wave analysis of ocean bottom seismometer records, *J. geophys. Res.,* **118**(6), 2878–2892.

Van Avendonk, H.J.A., Holbrook, W.S., Okaya, D., Austin, J.K., Davey, F. & Stern, T., 2004. Continental crust under compression: a seismic refraction

study of South Island Geophysical Transect I, South Island, New Zealand, *J. geophys. Res.,* **109**(B6), B06302, doi:10.1029/2003JB002790.

Wallace, L.M., Beavan, J., McCaffrey, R., Berryman, K. & Denys, P., 2007. Balancing the plate motion budget in the South Island, New Zealand using GPS, geological and seismological data, *Geophys. J. Int.,* **168**(1), 332–352.

Ward, K.M., Porter, R.C., Zandt, G., Beck, S.L., Wagner, L.S., Minaya, E. & Tavera, H., 2013. Ambient noise tomography across the Central Andes, *Geophys. J. Int.,* **194**(3), 1559–1573.

Wilson, C.K., Jones, C.H., Molnar, P., Sheehan, A.F. & Boyd, O.S., 2004. Distributed deformation in the lower crust and upper mantle beneath a continental strike-slip fault zone: Marlborough fault system, South Island, New Zealand, *Geology,* **32**(10), 837, doi:10.1130/G20657.1.

Yang, Y., Li, A. & Ritzwoller, M.H., 2008. Crustal and uppermost mantle structure in southern Africa revealed from ambient noise and teleseismic tomography, *Geophys. J. Int.,* **174**(1), 235–248.

Yang, Y., Ritzwoller, M.H., Levshin, A.L. & Shapiro, N.M., 2007. Ambient noise Rayleigh wave tomography across Europe, *Geophys. J. Int.,* **168**(1), 259–274.

Yao, H., Beghein, C. & van der Hilst, R.D., 2008. Surface wave array tomography in SE Tibet from ambient seismic noise and two-station analysis—II. Crustal and upper-mantle structure, *Geophys. J. Int.,* **173**(1), 205–219.

Zha, Y., Webb, S.C., Wei, S.S., Wiens, D.A., Blackman, D.K., Menke, W., Dunn, R.A. & Conder, J.A., 2014. Seismological imaging of ridge-arc interaction between the Eastern Lau spreading center from OBS ambient noise tomography, *Earth planet. Sci. Lett.,* **408,** 194–206.

Zheng, S., Sun, X., Song, X., Yang, Y. & Ritzwoller, M.H., 2008. Surface wave tomography of China from ambient seismic noise correlation, *Geochem. Geophys. Geosyst.,* **9**(5), doi:10.1029/2008GC001981.

Zheng, Y., Shen, W., Zhou, L., Yang, Y., Xie, Z. & Ritzwoller, M.H., 2011. Crust and uppermost mantle beneath the North China Craton, northeastern China, and the Sea of Japan from ambient noise tomography, *J. geophys. Res.,* **116**(B12), B12312, doi:10.1029/2011JB008637.

Zietlow, D.W., Sheehan, A.F., Molnar, P.H., Savage, M.K., Hirth, G., Collins, J.A. & Hager, B.H., 2014. Upper mantle seismic anisotropy at a strike-slip boundary: South Island, New Zealand, *J. geophys. Res.,* **119**(2), 1020–1040.

SUPPORTING INFORMATION

Supplementary data are available at *GJIRAS* online.

Figure S1. Ray density of group velocity models at (A) 8 s, (B) 16 s, (C) 25 s and (D) 35 s.

Figure S2. Resolution of group velocity models at (A) 8 s, (B) 16 s, (C) 25 s and (D) 35 s.

Figure S3. Root mean square misfit, represented as velocity (km s^{-1}), as a function of period for models parametrized with no anisotropy (isotropic), 2Ψ anisotropy and $2\Psi + 4\Psi$ anisotropy. Models are parametrized otherwise as described in the text. This figure demonstrates that the inclusion of 4Ψ anisotropy does not significantly improve the fit of our models to data as compared to models with only 2Ψ anisotropy.

Figure S4. An example of all of the realizations of the 1000 bootstrap iterations at a node near the centre of the array ($-44°$ latitude, $171°$ longitude) for the 16 s period map. Standard errors at a given node are calculated from at a node are calculated from these distributions. The standard errors calculated in this example, from the top to bottom plot, are 0.017 km s^{-1}, 0.28 per cent and 7.2°.

Figure S5. Anisotropy percent and fast direction as a function of anisotropic smoothing coefficient for 8 s (top), 16 s (middle) and 20 s (bottom) models at a point near the centre of our array (-44, -107). The isotropic smoothing coefficient was set to 250 in all cases,

consistent with the results presented in the paper. The anisotropic smoothing coefficient was allowed changed. These results demonstrate that the fast direction is consistent regardless of the smoothing while the amplitude of anisotropy is dependent on the smoothing chosen.

Please note: Oxford University Press is not responsible for the content or functionality of any supporting materials supplied by the authors. Any queries (other than missing material) should be directed to the corresponding author for the paper.